Available online at www.sciencedirect.com
SCIENCE DIRECT®
International Journal of Thermal Sciences 43 (2004) 315–329
International Journal of Thermal Sciences
www.elsevier.com/locate/ijts

A thermographic method to evaluate the local boundary layer separation phenomena on aerodynamic bodies operating at low Reynolds number

S. Montelpare [a,*], R. Ricci [b]

[a] *Università Politecnica delle Marche, Department of Energetics, Via Brecce Bianche, 60100 Ancona, Italy*
[b] *University of Chieti, D.S.S.A.R.R., Viale Pindaro 42, Pescara, Italy*

Received 20 May 2003; received in revised form 26 June 2003; accepted 1 July 2003

Abstract

This study uses infrared thermography to focus on local separation phenomena affecting the laminar boundary layer on aerodynamic bodies operating at low Reynolds numbers, and particularly on the laminar separation bubble that occurs, for instance, in applications such as gliders, microplanes and small windfarm turbines. The work was organized into several stages. First the reliability of the wind tunnel available at the Energetics Department of the "Università Politecnica delle Marche" was tested by comparing the results obtained on an Eppler 387 profile with data provided by other, similar tunnels for the same profile. Then the presence of a laminar bubble was ascertained using classic measuring methods, e.g., the spring balance and pressure distribution analysis. The thermographic apparatus was set up and recordings were made and compared with the trend of the pressure coefficient: coupling the data showed an excellent consistency in the identification of the bubble and confirmed the feasibility of using thermography for the non-invasive measurement of this phenomenon. The final phase of the study involved a preliminary attempt to obtain quantitative information from the thermographic images too: two quantities, L_S and B_E, were defined for this purpose and enabled a preliminary characterization of the behavior of the laminar bubble according to the angle of attack.

Keywords: Laminar bubble; Infrared thermography; Boundary layer separation; Low Reynolds number; Experimental; Airfoil; Wind turbine

1. Introduction

The aim of this study was to analyze the separation of the laminar boundary layer on aerodynamic bodies operating at low Reynolds numbers by means of infrared thermography. There are numerous studies in the literature on the topic, but the majority of them are dedicated to systems that work at high Mach and Reynolds numbers [1–7], while few papers focus on the aerodynamics of low Reynolds numbers [8–10] and this prompted us to fine adjust an experimental method [11–14] capable of detecting and quantitatively assessing local separation phenomena affecting the boundary layer, such as the laminar bubble. This phenomenon is conventionally assessable using techniques such as the dynamometric measurement of aerodynamic actions, the analysis of the pressure distribution on the body and, possibly, also flow visualizations using tracers.

1.1. The phenomenon studied

The laminar separation bubble (LSB) phenomenon can occur in numerous fields of application, such as gliders, microplanes, small windfarm turbines and, more in general, in profiles operating at low Reynolds numbers. This flow anomaly can occur on the surface of the body in the following conditions:

(1) a separation of the laminar boundary layer due to the presence of an adverse pressure gradient,
(2) a transition of the separated boundary layer,
(3) a turbulent reattachment downstream from the transition point.

In this case, a localized zone of virtually stationary recirculating flow forms on the surface of the body, which goes by the name of LSB (Fig. 1) and which modifies the pressure distribution around the wing profile, generating an increase in the aerodynamic resistance and a potential reduction in the wing's lift component.

* Corresponding author.
E-mail address: s.montelpare@ing.univpm.it (S. Montelpare).

1290-0729/$ – see front matter
doi:10.1016/j.ijthermalsci.2003.07.006

Nomenclature

B_E	bubble lengthwise dimension		
c	airfoil chord length	m	
C_l	section lift coefficient		
C_L	wing lift coefficient		
C_d	section drag coefficient		
C_D	wing drag coefficient		
$C_{m,c/4}$	section pitching moment coefficient		
$C_{M,c/4}$	wing pitching moment coefficient		
C_p	airfoil pressure coefficient		
D	drag	N	
h	convective heat transfer coefficient	$W{\cdot}m^{-2}{\cdot}K^{-1}$	
L	lift	N	
L_E	separation point distance from the leading edge		
L_T	bubble transition length		
L_S	bubble start point		
LBL	laminar boundary layer		
KBL	kinematic boundary layer		
M	moment	$N{\cdot}m$	
Nu	Nusselt number		
q_∞	free stream dynamic pressure		
Re	Reynolds number		
R_T	bubble turbulent reattachment point		
S	wing section planform area	m^2	
S_T	bubble laminar separation point		
Pr	Prandtl number		
ThBL	thermal boundary layer		
TBL	turbulent boundary layer		

Greek symbols

α	angle of attack	° degrees
δ_{kin}	kinetic boundary layer thickness	
δ_{therm}	thermal boundary layer thickness	
λ	thermal conductivity	$W{\cdot}m^{-1}{\cdot}K^{-1}$
μ	dynamic viscosity	$s{\cdot}m^{-2}$
ν	kinematic viscosity	$m^2{\cdot}s^{-1}$
ρ	density	$kg{\cdot}m^{-3}$

Subscripts

∞	conditions of the free stream
m	mean value

Superscripts

$'$	value referred to the airfoil section
w	conditions on the wall

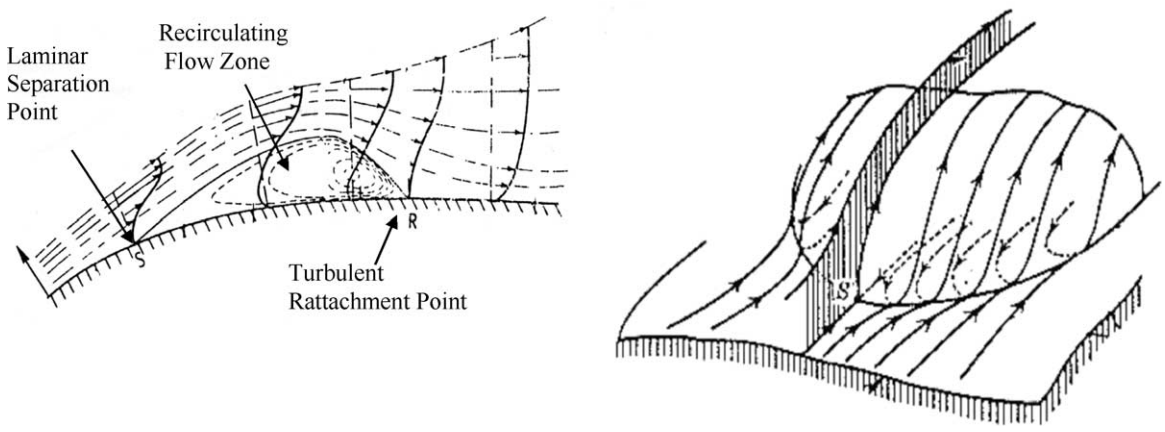

Fig. 1. Laminar bubble diagram.

At this stage of the research, our attention was focused on the laminar bubbles located on the extrados of a profile beyond 10% of the chord from the leading edge. If these LSB are situated around the midline of the extrados of a profile, they can induce a pre-stall type of hysteresis (Fig. 2): in fact, the laminar bubble initially forming at the midline of the chord where $\alpha \approx 0°$ will subsequently grow towards the trailing edge as the angle of attack increases and will induce bending in the curve C_L–α similar to the case of a stall from the trailing edge (Fig. 2a). Beyond a certain angle, the bubble will become smaller and will move towards the leading edge, increasing the lift coefficient. Finally, as α diminishes, the value of C_L will remain higher than the ascending curve until a critical value is reached, below which the bubble will become larger and the two curves will overlap again. Observing the Eiffel polar (Fig. 2b), we can see that there is an increase in the drag coefficient and a reduction in the aerodynamic efficiency in the area occupied by the bubble due to the effect of the hysteresis.

2. Experimental setup

All the tests were performed at the open-circuit wind tunnel installed at the Department of Energetics of the

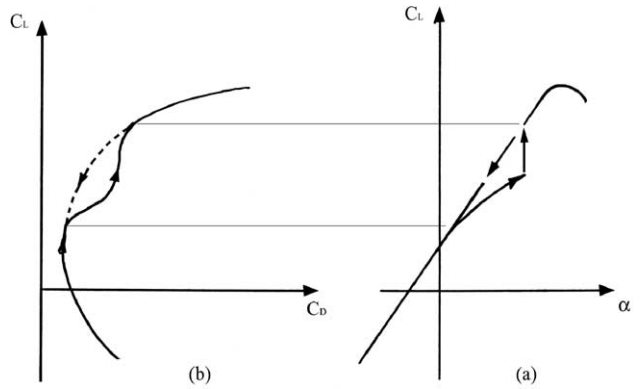

Fig. 2. Pre-stall hysteresis.

"Università Politecnica delle Marche" (Fig. 3). This tunnel is divided into three main parts:

(1) a convergent section, which has an area contraction ratio of 4.65,
(2) a closed test chamber 1.5 m long, 0.62 m wide and 0.38 m high,
(3) a divergent section, situated downstream from the test chamber, containing a 10-blade suction fan controlled by means of an inverter.

The maximum air velocity (Fig. 4a) at the vacuum test chamber's inlet is 30 [ms^{-1}] and the mean turbulence factor at the center of the section (Fig. 4b) is 0.3%. Both measurements, velocity and turbulence, are taken using a Dantec hot wire anemometric system.

Aerodynamic measurements were taken using a 6-axis spring balance and a Scanivalve 45-sensor pressure scanner: the former enables the measurement of lift (C_L), drag (C_D) and momentum ($C_{M,c/4}$); the latter is for the sequential analysis of the pressure distribution around the profile for a subsequent calculation of the lift, drag and momentum coefficients.

Thermographic measurements were taken using an AGEMA THV900 LW infrared camera (Fig. 5a) with a temperature resolution of 0.08 °C operating in a wavelength range between 8 and 12 micron. The profile is observed through an IR-transparent window provided on the top of the test chamber (Fig. 5b); the IR window is made of a sheet of polyethylene 10 micron thick with a transmission coefficient of 0.86 in the IR camera wavelengths.

The wing section is achieved by combining two fiber half-shells prepared in a mold; profiling of the molds is done with a cutting machine (Fig. 6a) that follows two profile templates obtained using numerical control.

The wing section for the thermographic and spring balance tests was metalized with a sheet of adhesive aluminium 25 micron thick and was subsequently coated with matte black paint; the layer of paint guarantees a lower reflection coefficient in the IR range than the polished aluminium and enables a measured emissivity of 0.94. A metal conductor was chosen for the surface coating because it enables the passage of electric current and the generation of a constant heating capacity due to the Joule effect; the input capacity is monitored using an adjustable current generator.

Fig. 3. Wind tunnel at the Energetics Department of the "Università Politecnica delle Marche".

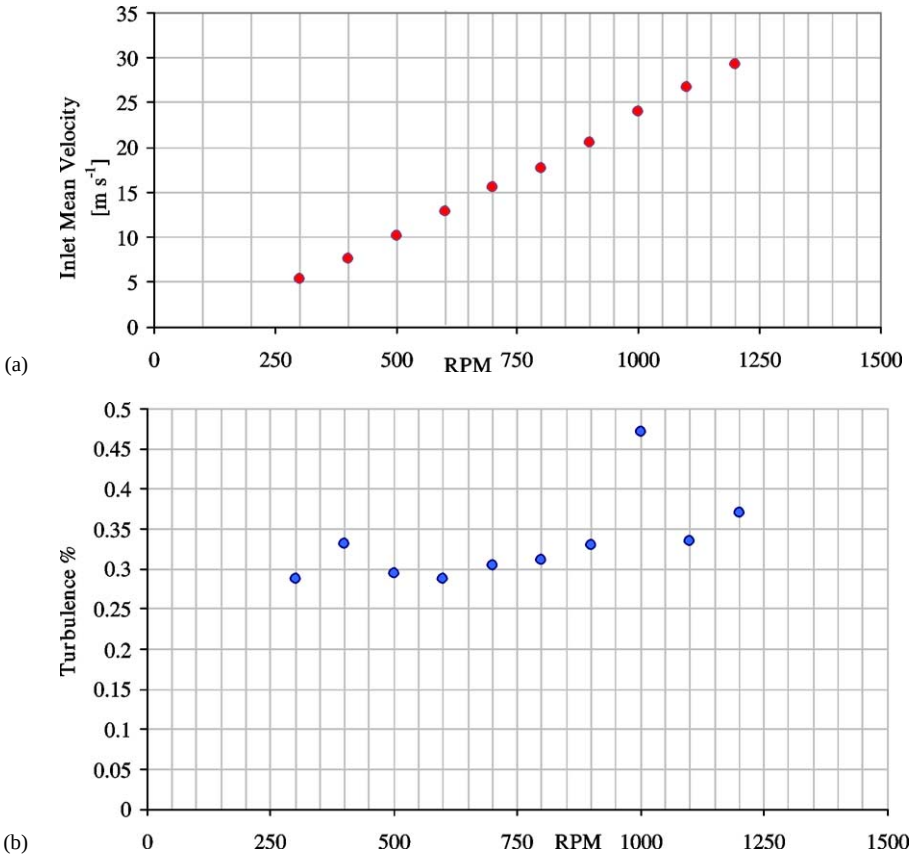

Fig. 4. Velocity (a) and turbulence (b) in the vacuum test section.

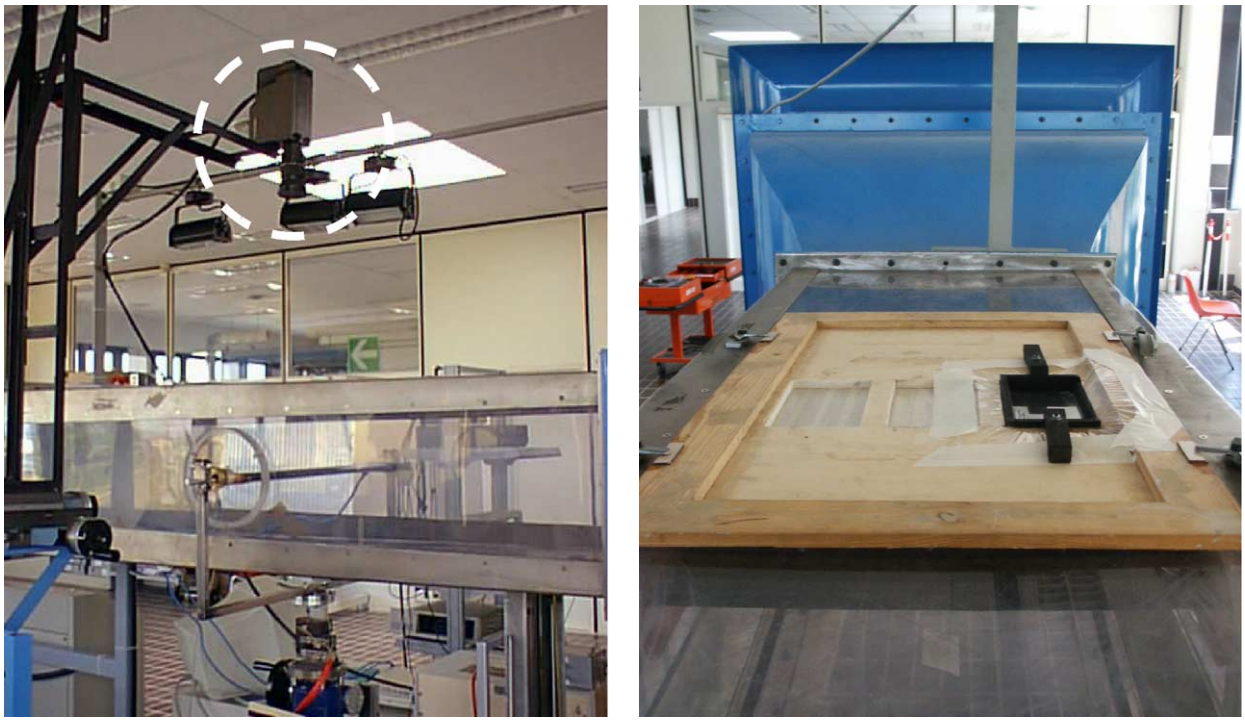

(a) (b)

Fig. 5. Thermographic machine (a); IR window (b).

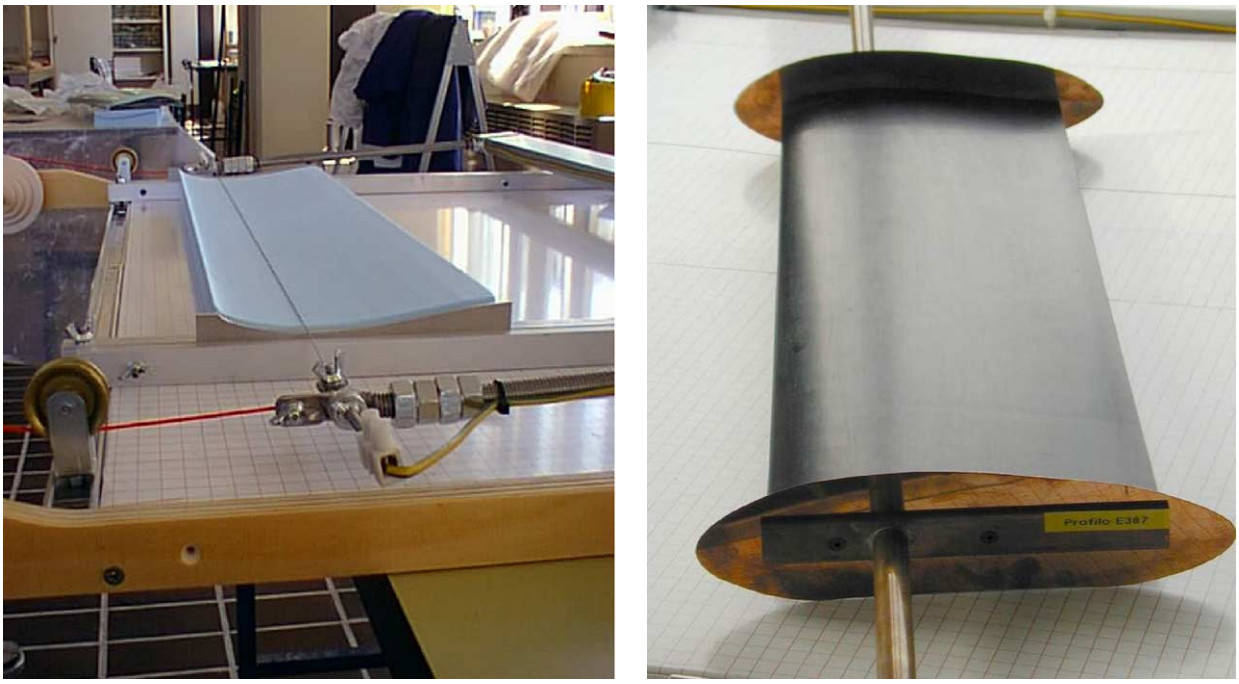

(a) (b)

Fig. 6. Machine for cutting the molds (a); Metalized wing profile (b).

3. Experimental results

Tests were performed on an Eppler 387 profile, which was chosen for two main reasons: first, because it reveals LSB phenomena at low Reynolds numbers; second, because numerous results are available for comparison in the literature, obtained in wind tunnels similar to the one used in the present case. To be precise, data obtained by the Aerodynamic and Gas Dynamics Institute of the University of Stuttgart and by the Department of Aeronautics and Astronautics Engineering of the University of Illinois were taken for reference. The wing profile parameter considered for the comparison was the trend of the lift coefficient.

3.1. Pressure sensor findings

Pressure coefficient analyses were performed at two different Reynolds numbers, 100k and 200k, and for angles of attack varying between $-5°$ and $14°$. The pressure readings were taken on 30 static sensors along the median section of the profile (Fig. 7).

Fig. 8 shows the trends of the pressure coefficient C_p on the extrados and intrados of the profile at the two Reynolds numbers considered. The findings show an increase in the suction peak on the nose of the profile as the angle of attack increases; for α values greater than $6°$, however, there is a reduction in the area affected by said peak (Fig. 8a), with a probable consequent reduction in the maximum C_L achievable. There is clearly (Figs. 8b–8c) also a constant pressure zone within the pressure recovery: this anomaly develops already for small negative angles and persists as the angle of attack increases up to approx. $10°$. The plateau shifts onto the extrados of the profile as the flow's angle of incidence varies and simultaneously modifies its longitudinal extension. Referring to the information in the literature, this anomaly can be brought down to a laminar bubble that induces a constant internal pressure due to the virtually stationary recirculation.

Fig. 9 shows the trends of the curves C_l–α and C_d–α obtained by integrating the pressure distribution around the profile at the various angles of attack. The first item worthy of note is the null lift angle of $-3°$, consistent with what we know about the E387 from the literature. Secondly, there is a change of gradient in the curve C_l–α for an angle of approx. $-1°$. Based on the above considerations, this might be due to a large laminar bubble inducing bending in the lift curve with a pre-stall type of hysteresis. Observing the curve C_d–α apparently provides no information concerning the presence of a bubble, as in the case of lift, though it does show an inflexion for an angle of approx. $5°$ with an increase in the drag in the range $3°$–$7°$.

The change of gradient and the inflexion, together with the constant pressure zones, seem to confirm the presence of a laminar bubble on the tested profile.

There is a further point to note on the lift diagram in relation to the anomalies in the stall zone: there are oscillations probably attributable to the limited number of sensors in the nose zone, or to problems relating to the way the test section was fixed.

The graphs in Fig. 10 show the results for the lift coefficient (obtained from the distribution of the C_p) combined with the findings recorded at the other, previously-

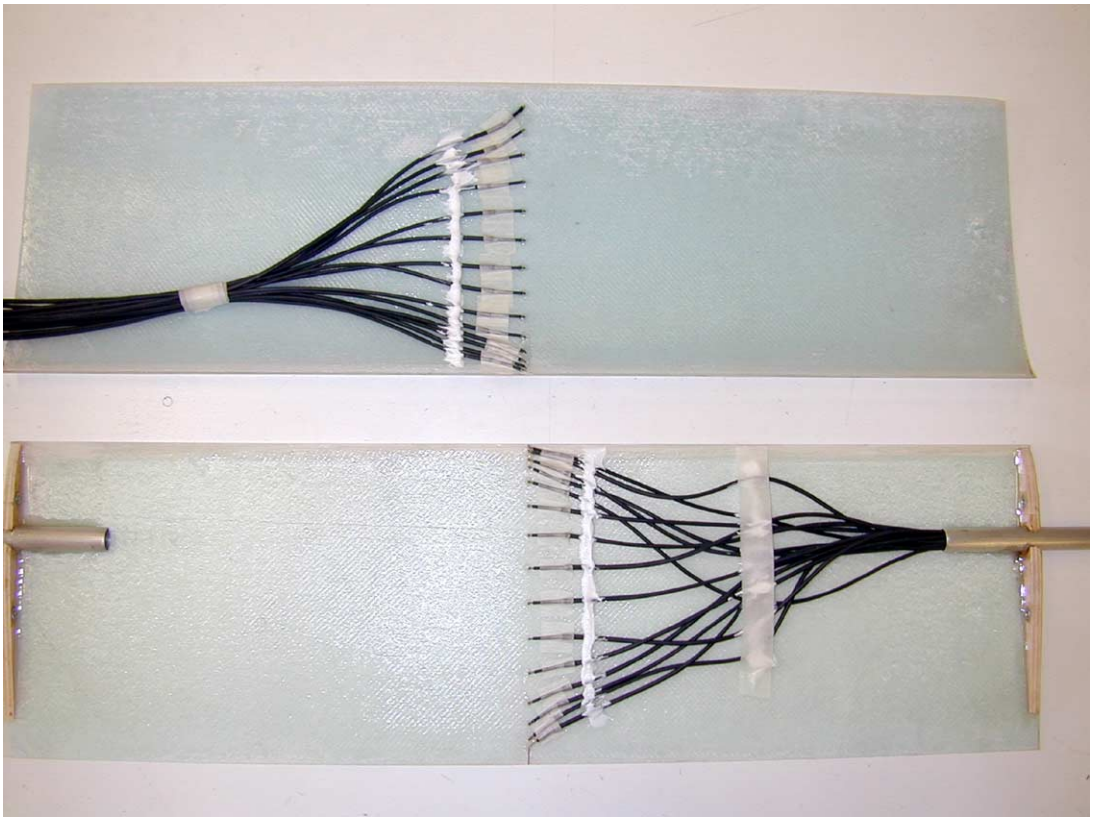

Fig. 7. Arrangement of the static pressure sensors.

mentioned wind tunnels and with the results obtained using two numerical models widely used in aerodynamics, i.e., Xfoil and Visualfoil: these data confirmed the validity of the wind tunnel used in our study: the null lift angle of $-3°$ was consistent with the value for the Stuttgart tunnel and only slightly lower than the findings at the University of Illinois and the numerical simulations ($-3°$ vs. $-3.75°$). In addition, the gradient of the lift curve was the same for all the data and substantial differences were only observable in the region in the vicinity of the stall, which could not be unequivocally determined from the available data anyway. Further comparisons using the other Reynolds number we tested produced similar results, so the findings obtained at the "Università Politecnica delle Marche" wind tunnel can be considered reliable, at least up to the angles prior to stalling.

3.2. Spring balance findings

Spring balance tests were also conducted on the E387 profile at the same Reynolds numbers and at the same angles (Fig. 11). In this case, the curve C_L showed a slightly different null lift angle, i.e., $-2.5°$, due to the relative sensitivity of the spring balance for small angles of attack, where the absolute drag and lift values are low and the error in their assessment is consequently high; indirect confirmation of this comes from the observation of the error bands, that drop dramatically when higher Reynolds numbers and greater forces are considered.

On the other hand, the lift curve confirms the change of gradient for an angle of approx. $-1°$ and a maximum C_L value of the same order as in the analysis with the C_p. In this case, the Eiffel polar provides more information on the potential presence of a laminar bubble: in fact, there is a marked increase in the drag in the range $-1°$ to $9°$.

Both conditions, i.e., the bending of the curve C_L–α and the increase in the C_D, are signs of the presence of an LSB and, referring to the results obtained previously with the analysis of the C_p, the presence of such a separation phenomenon on the profile in question is therefore confirmed.

3.3. Thermographic findings

Once the reliability of the wind tunnel and the presence of an LSB on the wing profile in question had been verified, thermographic measurements were performed.

Before going on to analyze the results, it is worth explaining the hypotheses adopted and what should happen thermographically in the event of a local separation of the boundary layer. Exploiting the Reynolds analogy, we can see first of all that, in forced air convection conditions, the behavior of the thermal boundary layer (ThBL) is closely related to that of the kinematic boundary layer (KBL), and their thickness increases in the same way; the most immediate consequence of this close relationship is that an anomaly in the KBL, e.g., a laminar bubble, must

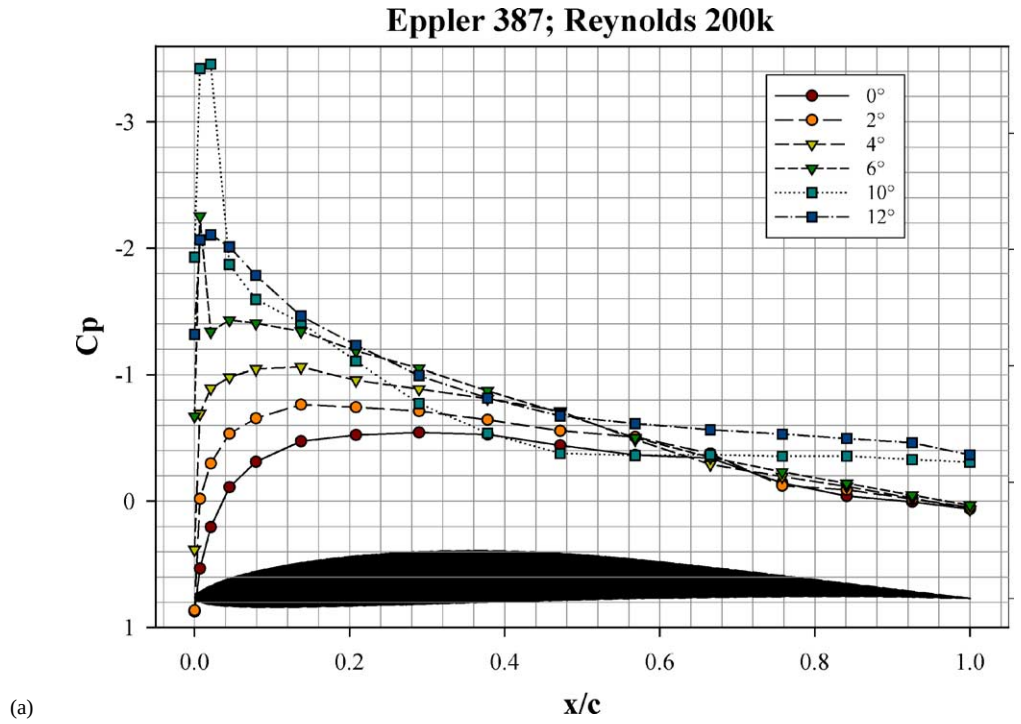

(a)

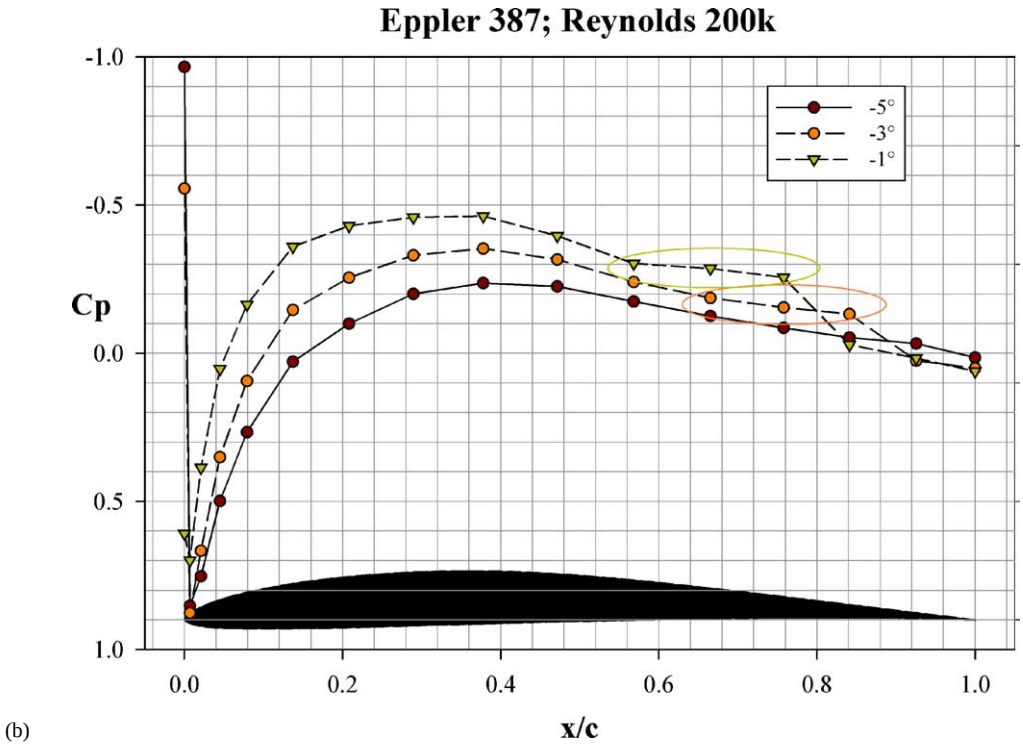

(b)

Fig. 8. Pressure trends around the wing profile: extrados Re200k (a); intrados Re200k (b); extrados Re100k (c).

be reflected in a corresponding anomaly in the ThBL. In constant and unseparated boundary layer conditions, the trend of the surface temperature will rise in the direction of the flow and there will only be a discontinuity in the vicinity of the passage from laminar to turbulent flow, with the temperature suddenly dropping and then rising again (Fig. 12a). If there is an LSB, however, the near-stationary recirculation of the air it contains would induce a marked drop in the convective heat exchange coefficient and a consequent local increase in temperature; in the longitudinal distribution of the latter quantity, we would therefore see an initial discontinuity at the point of laminar separation,

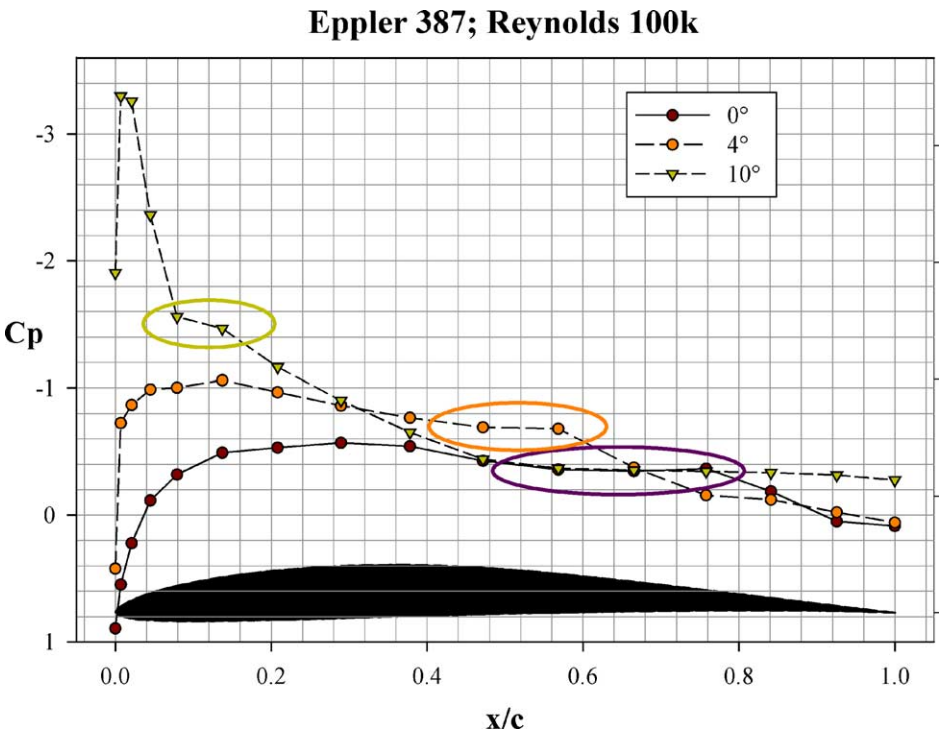

(c)

Fig. 8. Continued.

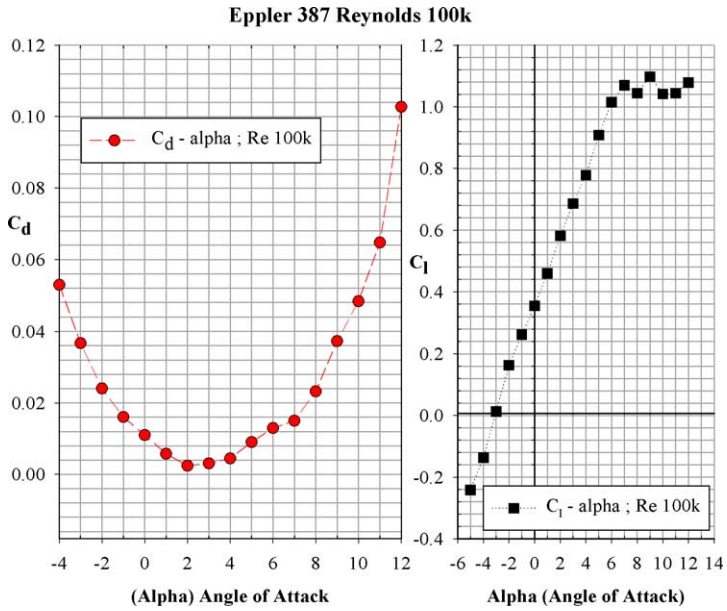

Fig. 9. C_d–α and C_l–α curves obtained by analyzing the C_p for Re 100k.

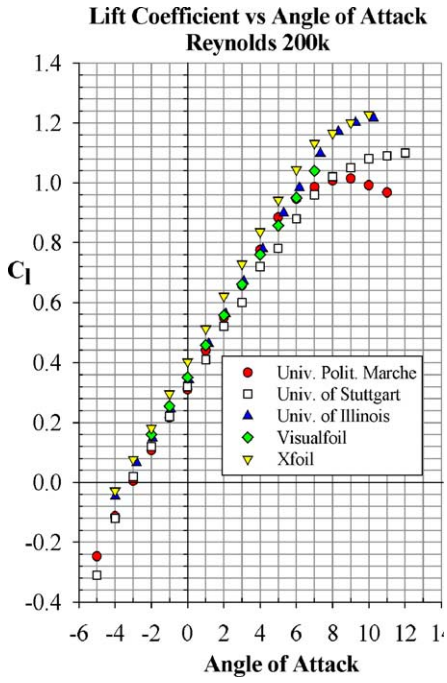

Fig. 10. Comparison with the other tunnels.

where the free shear layer forms, and a second discontinuity at the point of turbulent reattachment, corresponding to a jet impingement (Figs. 12b–12c).

The thermographic images obtained at both Reynolds numbers are shown in Figs. 13 and 14. The electrical energy delivered to the aluminium sheet is the same and there is an immediately apparent reduction in the surface temperature gradient at the higher Reynolds number that becomes greater the higher the value of the convective heat exchange coefficient.

In both cases, the images show zones with a higher local temperature on the extrados of the profile that change in lengthwise dimension and position as the angle of attack varies; beyond an angle of 7° there is also a change in

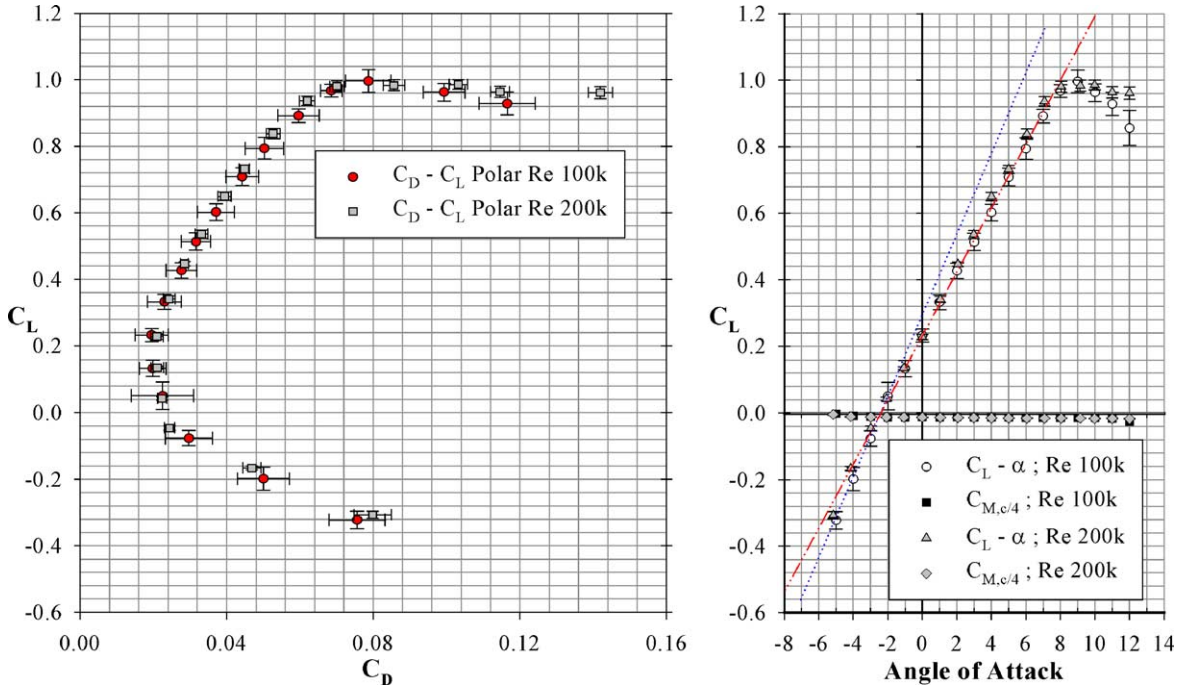

Fig. 11. Eiffel polar diagrams and C_L–α curves obtained with the spring balance for Re 100k.

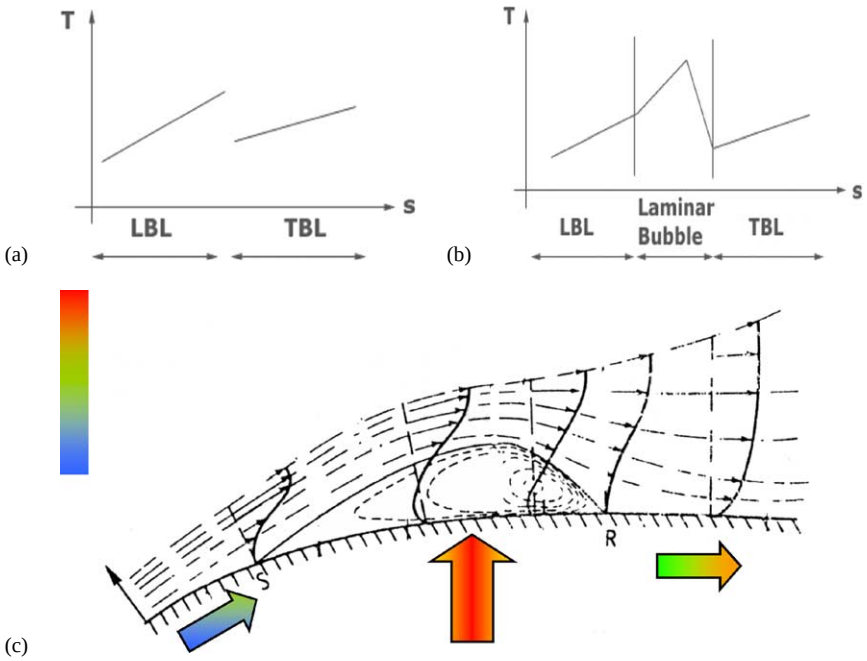

Fig. 12. Temperature trends on the wing profile: in the unseparated case (a); in the case of a bubble (b,c).

the crosswise dimension of the warmer zone that finally disappears for an angle of 10°.

Referring to our previous considerations, the warmer area can be explained by the presence of an LSB; this is confirmed by superimposing the findings of the pressure sensors and the results obtained with the Xfoil software on the thermographic data acquired at the same angles and Reynolds numbers.

Fig. 15 superimposes these data for both negative and positive angles; there is obviously a good consistency between the numerical data produced by Xfoil and the experimental findings obtained by the pressure sensors. It is also clear that the constant pressure plateau zones corresponding to a laminar bubble coincide with the locally warmer areas. This correspondence persists at the various angles of attack considered and at both Reynolds numbers,

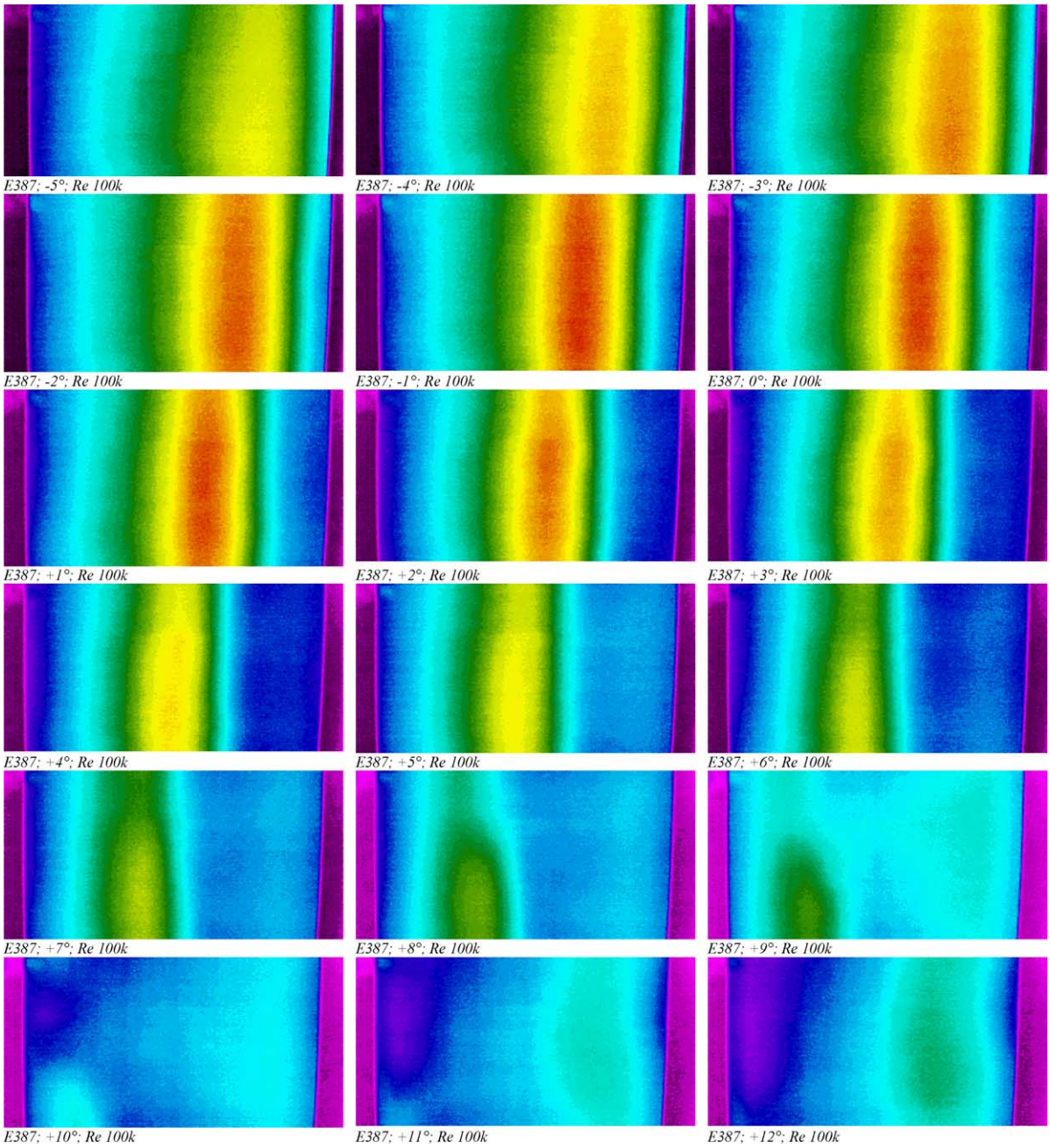

Fig. 13. Eppler 387 thermographic images at Reynolds 100k.

thus confirming the validity of the thermographic system in identifying the LSB phenomenon.

The point of turbulent reattachment is fairly easy to identify already from a qualitative standpoint, since the surface temperature undergoes an abrupt reduction due to jet impingement. Conversely, the laminar separation zone is more difficult to pinpoint because the rise in temperature caused by the formation of the free shear layer is not so great. This made it necessary to perform a quantitative analysis to enable a more objective assessment of the laminar bubble's characteristic points (laminar separation, transition and turbulent reattachment). This was done by analyzing the first derivative of the second order at 5 points on the temperature profiles in the direction of the flow (Fig. 16), thereby further emphasizing the discontinuities from the maximum, minimum and zero points.

Having identified said points, we can define two quantities: the position where the bubble starts (L_S) and its lengthwise dimension (B_E). The first quantity, expressed as a percentage of the chord, is defined as the distance between the leading edge of the profile and the point of laminar separation of the boundary layer; the second quantity, which is again expressed as a percentage of the chord, is the distance between said point of separation and the point of turbulent

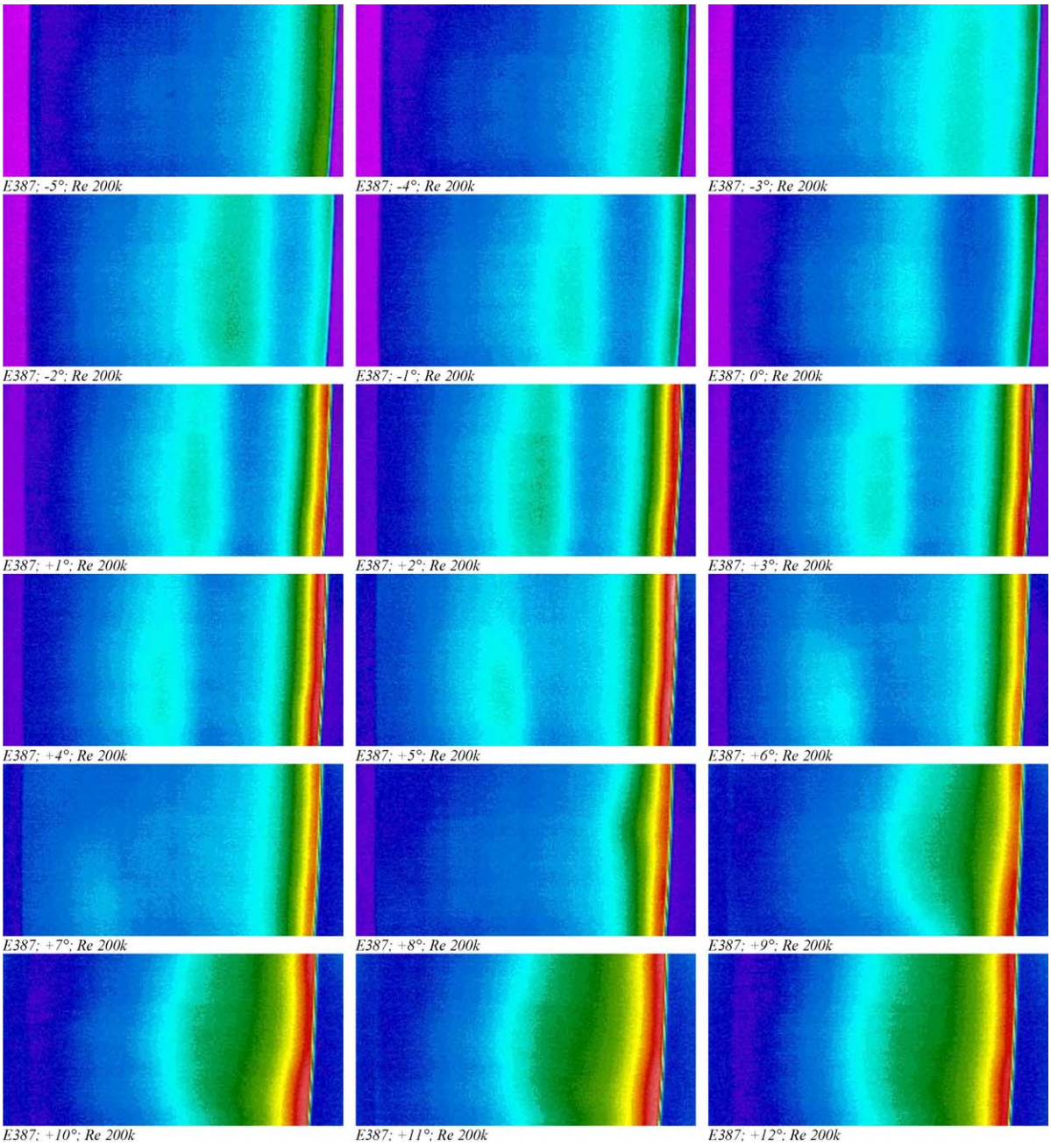

Fig. 14. Eppler 387 thermographic images at Reynolds 200k.

reattachment. These two quantities enable us to describe the behavior of the bubble according to the angle of attack and the Reynolds number.

Fig. 17 shows the trends of L_S and B_E obtained both by thermography and by the Xfoil numerical model at various angles of attack. Clearly, the point of laminar separation remains around 50% of the chord up to an angle of 0° and then shifts continuously towards the leading edge of the profile; at the same time, the dimension of the bubble seems to remain the same for negative angles and begins to diminish as soon as we reach alpha values greater than zero. Unlike the situation for the separation point, however, the dimension of the bubble presents a constant stretch for angles coming between $+3°$ and $+6°$; this means that the bubble merely moves towards the leading edge in this alpha range, whereas at the other angles of attack the displacement is accompanied by a reduction in its size.

Theoretically, the counterflow displacement of the point of separation can be correlated with the fact that it depends strictly on the adverse pressure gradient and the latter shifts towards the leading edge as the angle of attack increases. The trend of the quantity B_E is not so easy to explain, how-

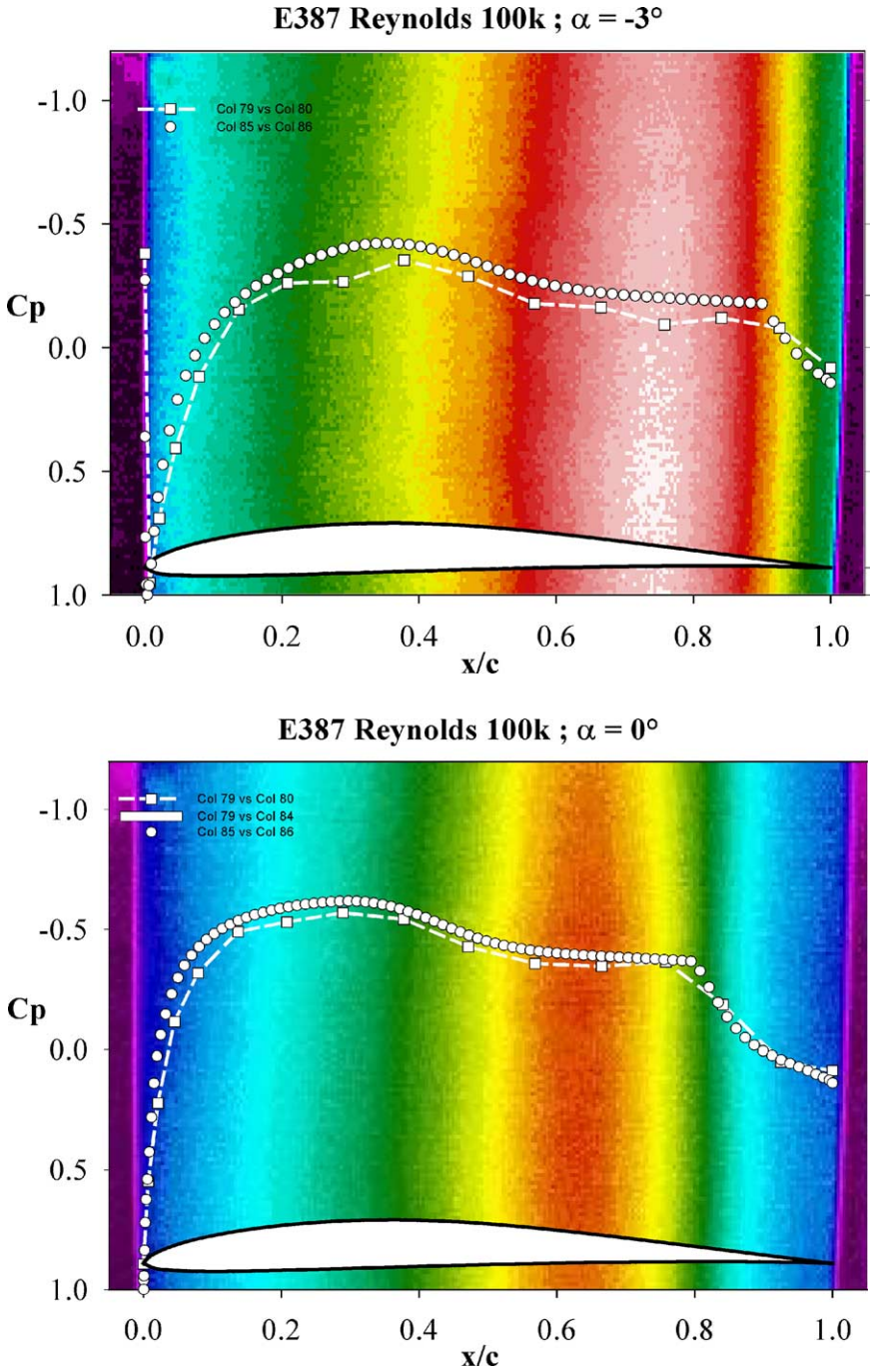

Fig. 15. Experimental and numerical C_p superimposed on the thermographic results.

ever, since it depends strictly on two parameters, i.e., the local Reynolds number and the adverse pressure gradient. We can safely say that the increase in the local Reynolds number induces an earlier transition of the separated boundary layer and an earlier turbulent reattachment, with a consequent reduction in the dimensions of the bubble, but it is impossible to say how the local Reynolds number correlates with the adverse pressure gradient, so it is also impossible to predict the exact behavior of the quantity B_E.

Fig. 17 also shows a good consistency between the numerical data produced by Xfoil and the thermographic test findings in relation to the behavior of the laminar separation point; vice versa, there is a significant difference in the absolute values of the dimension B_E, though the trend is the same. This is because the Xfoil software uses the en method to identify the separated boundary layer's point of transition and the values predicted by the numerical model are systematically higher than the thermographic measurements, with

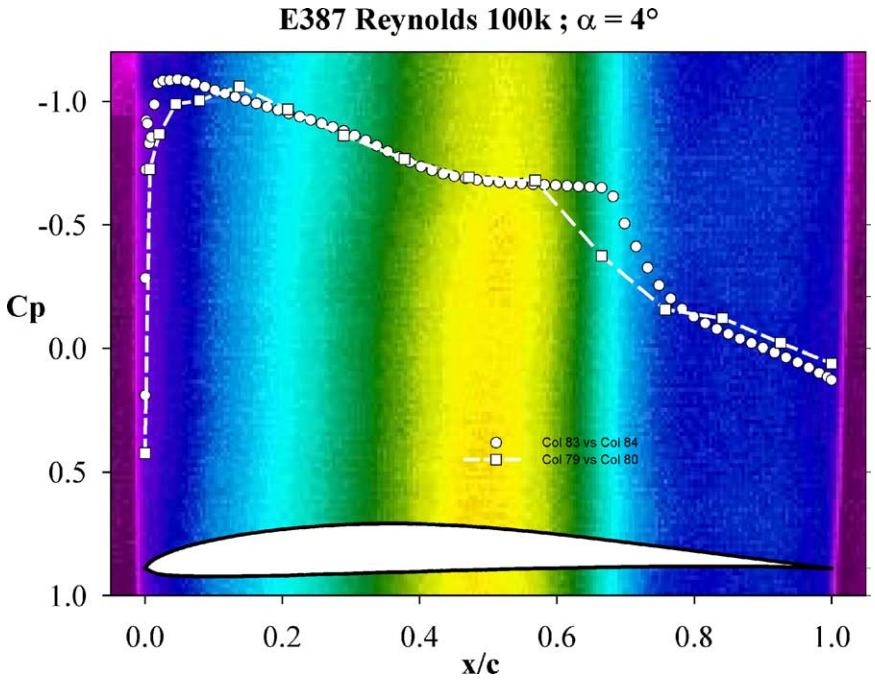

Fig. 15. Continued.

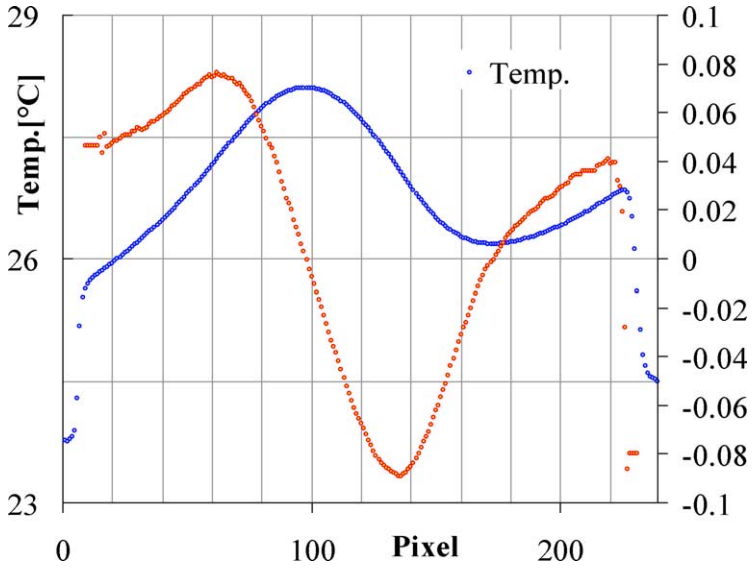

Fig. 16. Study of the first derivative of the temperature in a direction parallel to the flow.

a consequent displacement further downstream of the turbulent reattachment and an increase in the longitudinal dimension of the bubble.

4. Conclusions

The aim of the present study was to use IR thermography to evaluate the laminar separation bubble phenomenon on aerodynamic bodies operating at low Reynolds numbers. The experimental findings obtained on this wing profile validate the equipment available at the Department of Energetics of the "Università Politecnica delle Marche". The first tests performed on the E387 profile, using a spring balance and a pressure scanning system confirmed the presence of a sizable LSB situated around the midline of the profile for angles of attack nearing 0°; as alpha increased, the bubble seemed to persist and the pressure distribution indicates its displacement towards the leading edge.

Thermographic measurements of the heated profile showed locally warmer zones on the extrados; superimposing the pressure trends on the thermographic data showed that said zones corresponded to the laminar bubble, which induces a lower convective heat exchange coefficient. As

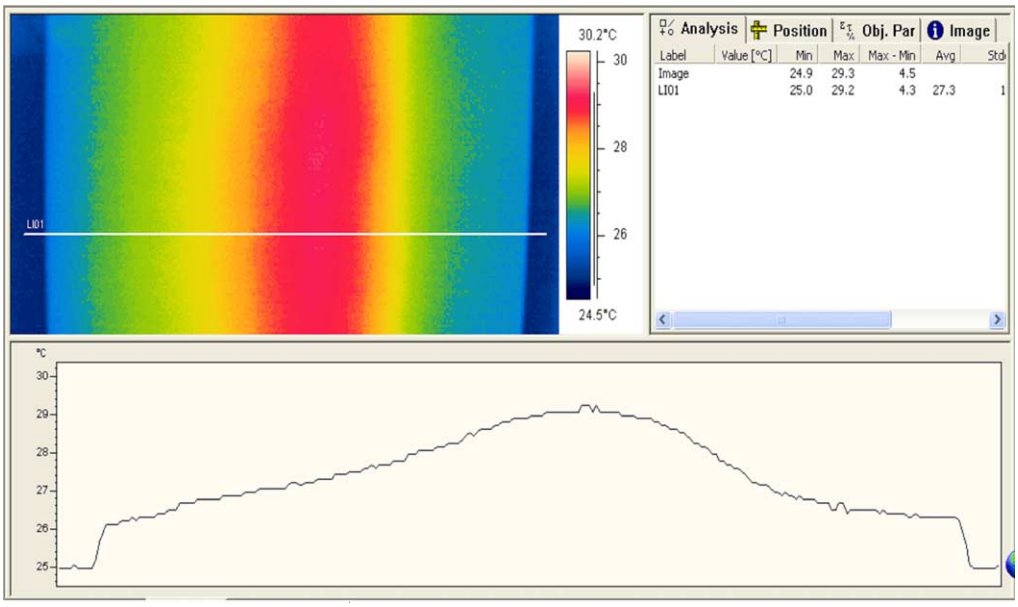

Fig. 16. Continued.

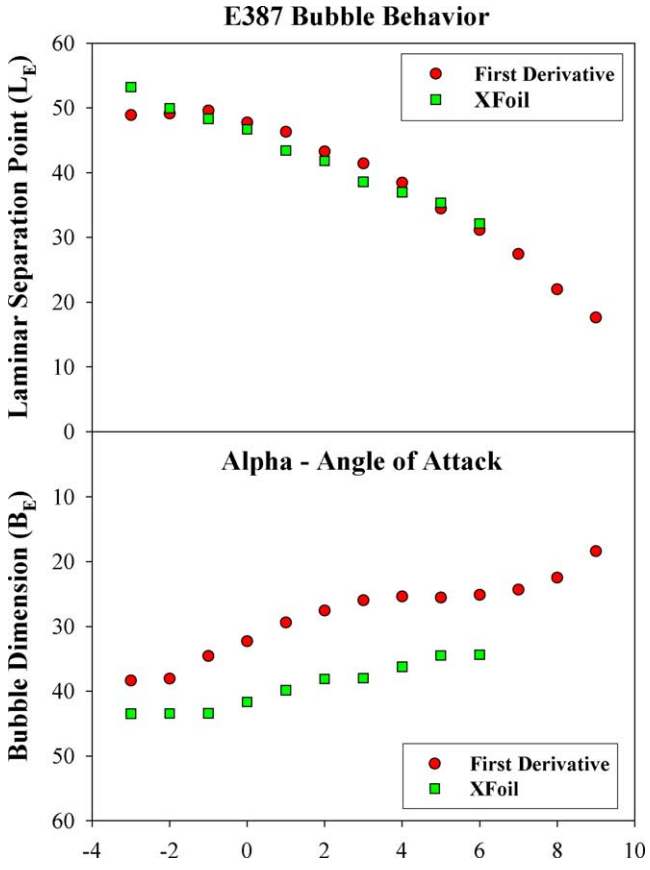

Fig. 17. Bubble behavior according to angle of attack.

a result, IR thermography was shown to represent a valid non-invasive measuring system capable of accurately identifying local boundary layer separation phenomena in real time.

Quantitative information from the thermographic images by means of a study of the first derivative of the temperature on the extrados of the profile enabled us to identify the points characterizing the bubble (i.e., the points of laminar separation, transition and turbulent reattachment). We defined two quantities L_S and B_E, that respectively represent the distance of the separation point from the leading edge and the longitudinal dimension of the bubble. Observing these quantities it is possible to notice that the bubble shifted gradually towards the leading edge, simultaneously diminishing in size the higher the value of alpha.

Acknowledgements

This work has been supported by CB Ricerca 60% ‘98 found, titled “Analisi numerica e termofluidodinamica di fenomeni di separazione di flusso in profili alari a bassi numeri di Reynolds”.

Appendix

$$C_l = \frac{L'}{q_\infty c} \quad \text{section lift coefficient}$$

$$C_d = \frac{D'}{q_\infty c} \quad \text{section drag coefficient}$$

$$C_{m,c/4} = \frac{M'}{q_\infty c^2} \quad \text{section pitching moment coefficient}$$

$$C_L = \frac{L}{q_\infty S} \quad \text{wing lift coefficient}$$

$$C_D = \frac{D}{q_\infty S} \quad \text{wing drag coefficient}$$

$$C_{M,c/4} = \frac{M}{q_\infty S c} \quad \text{wing pitching moment coefficient}$$

References

[1] D.S. Bynum, F.K. Hube, M. Keyc, P.M. Diek, Measurement and mapping of aerodynamic heating with an infrared camera, AEDC Rep. TR-76-54, 1976, 1–33.
[2] A.M. Bouchardy, G. Durand, G. Gauffre, Processing of infrared thermal images for aerodynamic research, in: SPIE Int. Technical Conference, April 18–22, Genova, Italy, vol. 1, 1983.
[3] R. Monti, Thermography in Flow Visualization and Digital Image Processing, Proc. Lect. Ser. Von Karman Institute for Fluid Dynamics, 1986.
[4] A. Quast, Detection of transition by infrared image technique, ICIASF 1987 Record (1987) 125–134.
[5] G.M. Carlomagno, L. De Luca, G. Buresti, G. Lombardi, Characterization of boundary layer conditions in wind tunnel tests through IR infrared thermography imaging, in: T.L. Williams (Ed.), Applications of Infrared Technology, in: Proc. SPIE, vol. 599, 1988, pp. 23–29.
[6] G.M. Carlomagno, L. De Luca, Infrared thermography in heat transfer, in: W.I. Young (Ed.), Handbook of Flow Visualization, Hemisphere, 1989, pp. 531–533, Ch. 32.
[7] K. Daryabeigi, W. Alderfer, S.E. Borg, Wind tunnel and flight flow visualization using infrared imaging, in: Proc. 37th Internat. Instrumention Symposium—Aerospace Industries Division, 1991, pp. 303–312.
[8] J.M. Brandon, G.S. Manuel, R.E. Wrigth Jr., B.J. Holmes, In-flight visualization using infrared imaging, J. Aircraft 27 (6) (1990).
[9] M.S. Selig, J.F. Donovan, D.B. Fraser, Airfoils at Low Speeds, Soartech 8, H.A. Stokely Publisher, 1989.
[10] C.A. Lyon, A.P. Broeren, P. Giguère, A. Gopalarathnam, M.S. Selig, Summary of Low-Speed Airfoil Data, vol. 3, Soartech Publications, Virginia Beach, Virginia, 1997.
[11] S. Montelpare, M. Paroncini, R. Ricci, P. Zazzini, Flow visualization of the laminar separation bubble by infrared thermography investigations, in: 5th Internat. Workshop on Advanced Infrared Technology and Applications, Venezia, 29–30 September, 1999.
[12] G. Latini, S. Montelpare, R. Ricci, Individuazione di fenomeni di separazione dello strato limite su corpi aerodinamici operanti a bassi numeri di Reynolds mediante l'uso della Termografia, in: 6° Convegno Nazionale di Ingegneria del Vento In-Vento 2000, Genova, 18–21 giugno, 2000.
[13] S. Montelpare, R. Ricci, P. Zazzini, Laminar separation bubble visualisation by I.R. thermography, in: 9th International Symposium on Flow Visualization, Edinburgh, Scotland, 22–25 August, 2000.
[14] G. Cesini, S. Montelpare, R. Ricci, P. Zazzini, Un metodo termografico per lo studio del fenomeno di separazione dello strato limite laminare in corpi operanti a basso numero di Reynolds, in: 56° Congresso Nazionale ATI, Napoli, 10–14 settembre, 2001.